PAPER

Check for updates

Vortex-fluidic-mediated phase separation of polyethylene glycol and aqueous potassium phosphate characterised by real-time neutron imaging and scattering

Xuan Luo, [a] Ahmed H. M. Al-Antaki, [b] Andrew E. Whitten, [c]
Filomena Salvemini, [c] Evgenia Leivadarou, [d] Wei Zhang, [e] Harshita Kumari [fg]
and Colin L. Raston *[a]

The phase separation of polyethylene glycol (PEG) and aqueous potassium phosphate is slow under conventional batch processing. Herein, we investigate the instantaneous phase separation of this system through thin film shearing in a vortex fluid device (VFD), monitored in real time using *in situ* small-angle neutron scattering (SANS) and neutron imaging. The SANS data for the aqueous two-phase system (ATPS) are best fitted with the Debye model, indicating that PEG molecules adopt a Gaussian coil structure under shear in the presence of potassium phosphate. Notably, when mixed in the VFD, the radius of gyration (R_g) of PEG molecules differed from that observed under diffusion-controlled conditions in a stationary cuvette. Shearing in the presence of potassium phosphate further altered the Gaussian coil structure of PEG, as indicated by a decrease in R_g. Real-time monitoring of PEG structural changes in both monophasic and biphasic systems has thus been established. This approach is important for understanding fluid regimes and their applications in biphasic purification and beyond.

1 Introduction

Polyethylene glycol (PEG) and salt aqueous two-phase systems (ATPSs) have attracted considerable attention for the purification of biological materials such as proteins,[1] and some ATPSs have even been scaled up to industrial levels. For example, formate dehydrogenase has been isolated from 30–50 kg of wet *Candida boidinii* cells[2] and the separation of an amphiphilic fusion protein (EGIcore-HFBI) has been performed on a scale of up to 1200 L.[3] The PEG/salt ATPS is a commonly used separation technology due to its low cost and the low viscosity of both phases.[4] The phase separation rate of ATPSs is a critical factor that can be affected by various system parameters, including the

density and viscosity of each phase, and the interfacial tension between phases.[4] Some techniques can be applied to facilitate this phase separation process, one of which is through a vortex fluidic device or VFD.[1] We have demonstrated that the phase separation of PEG and potassium phosphate in VFD was facilitated,[1] regardless of the other biphasic system parameters. The VFD, which is a thin film microfluidic platform, consists of a rapidly rotating quartz tube (20 mm O.D., 17.5 mm I.D.), usually operated at ≤9000 rpm and an optimal tilt angle θ of +45° relative to the horizontal position.[5] Shear stress induced in the complex fluid flow in the liquid thin film has been harnessed for a number of applications. For example, we used the VFD to efficiently purify a microalgae-derived protein (C-phycocyanin or C-PC), achieving a 9.3-fold increase in phase separation efficiency, along with a 1.18-fold improvement in C-PC purity, and a 1.22-fold increase in yield compared to conventional non-VFD batch processing.[1] The VFD has also been used to exfoliate graphite and boron nitride,[6] laterally slice nanotubes despite their remarkably high tensile strength,[7–9] fabricate protein macroporous spheres,[10] and enhance enzymatic reactions.[11]

Although phase separation phenomena have been observed in VFD-related studies[1,12] and fluid flow models have been developed for organic solvent-based liquid biphasic systems,[13] the behaviour of polymer-based liquid biphasic systems is poorly understood. Shear stress in the VFD arises from

[a]Flinders Institute for Nanoscale Science and Technology, College of Science and Engineering, Flinders University, Adelaide, SA 5042, Australia. E-mail: colin.raston@flinders.edu.au

[b]Department of Chemistry, Faculty of Science, University of Kufa, Najaf 54001, Iraq

[c]Australian Nuclear Science and Technology Organisation, New Illawarra Rd, Lucas Heights, NSW 2234, Australia

[d]Department of Applied Mathematics and Theoretical Physics, University of Cambridge, CB3 0WA, UK

[e]Centre for Marine Bioproducts Development, College of Medicine and Public Health, Flinders University, Adelaide, SA 5042, Australia

[f]James L. Winkle College of Pharmacy, University of Cincinnati, 231 Albert Sabin Way, MSB 3109 C, Cincinnati, Ohio 45221, USA

[g]Materials Science and Engineering, College of Engineering and Applied Science, University of Cincinnati, 2901 Woodside Drive, Cincinnati, Ohio 45221, USA
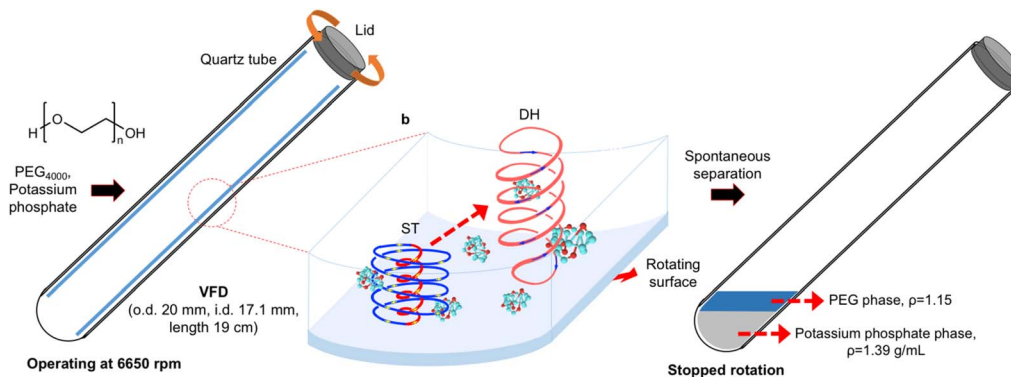
Fig. 1 Schematic of the VFD operated in a confined mode at $\theta = +45°$ and 6550 rpm. During operation, spinning top (ST) and double helical (DH) topological fluid flows occur in the tube, providing good mixing of the PEG$_{4000}$ and aqueous potassium phosphate phases. After VFD processing, the two phases spontaneously separate, with the PEG phase on top of the potassium phosphate phase.

topological fluid flows, including a coriolis-induced spinning top (ST) flow, a double helical (DH) flow across the liquid thin film, or a combination of both flow types (Fig. 1).[13,14] Neutrons, which are strongly attenuated by hydrogen, are ideally suited for imaging hydrogen-rich fluids and provide a non-destructive method for direct imaging of mixing in a two-phase system.[15] In the VFD, the enhanced nano-encapsulation of fish oil,[16] breaking of flourous bis-urea gels,[17] and the structure of phospholipids in aqueous media under shear have been probed *in situ* using small-angle neutron scattering (SANS).[18] Herein, *in situ* SANS measurements were used to investigate the two-phase system based on PEG and aqueous potassium phosphate in the VFD, focusing on the structure and interaction characteristics of PEG molecules during mixing. Neutron imaging was applied to visualise the biphasic system during VFD processing.

2 Materials and methods

PEG$_{4000}$ (polyethylene glycol with an average molecular weight of 4000 g mol^{-1}), dipotassium hydrogen phosphate (K$_2$HPO$_4$), and potassium dihydrogen phosphate (KH$_2$PO$_4$) were purchased from Sigma-Aldrich. All chemicals were of analytical grade. For SANS measurements, the samples were prepared one day in advance and left to equilibrate without filtration. D$_2$O was used to achieve sufficient scattering contrast between the sample and liquid carrier while also minimizing the incoherent scattering background from hydrogen.[19] Aqueous potassium phosphate was prepared according to Luo *et al.*[1] by mixing K$_2$HPO$_4$ and KH$_2$PO$_4$ at a ratio of 1.82 : 1. An ATPS of PEG$_{4000}$ and aqueous potassium phosphate was prepared using the previously reported optimum condition for C-PC purification.[1] A stock solution of PEG was prepared by dissolving 10 g of PEG$_{4000}$ in 10 g of D$_2$O, and a stock solution of potassium phosphate was prepared by dissolving 2.9 g of K$_2$HPO$_4$ and 1.6 g of KH$_2$PO$_4$ in 10.5 g of D$_2$O. A typical 10 g ATPS system consisted of 1.3 g of PEG$_{4000}$ (stock), 4.5 g of potassium phosphate (stock), and 4.2 g of D$_2$O, giving final mass fractions (w/w) of 6.4% and 13.5% for PEG and potassium phosphate, respectively. When this ATPS was applied to C-PC purification, 4.2 g of C-PC suspension was used.

For all *in situ* experiments, the quartz tube (20 mm in diameter, 17.5 mm internal diameter) in the VFD was set at a tilt of +45°, which is the optimal angle for most processes in the device, as substantiated by temperature and mixing time changes in liquid thin films.[13,17] SANS measurements were performed using the BILBY time-of-flight (ToF) SANS instrument at the Australian Centre for Neutron Scattering at the Australian Nuclear Science and Technology Organisation (ANSTO), Lucas Heights, Australia. All measurements were carried out at room temperature, using either a quartz cell with a 2 mm path length or a rotating quartz VFD tube. The centre of the neutron beam passed though the tube at a point 3 cm from the bottom. The neutron wavelength (λ) range of 2–18 Å with a wavelength resolution ($\Delta\lambda/\lambda$) of 0.12, covering a momentum transfer range of 0.01 Å^{-1} < q < 0.35 Å^{-1}. Scattered neutrons were detected with a 640 × 640 mm rear detector positioned 7.000 m from the sample, and four curtain detectors each with dimensions of 320 × 640 mm with one pair were positioned 3.500 m from the sample, and the other pair at 4.500 m from the sample. The measurement time was 1 h for all samples and solvents. All SANS data were corrected for transmission and background radiation, before being reduced to $I(q)$ *vs. q* profiles and placed on an absolute scale using the empty beam neutron flux and the sample thickness, before subtracting background scattering from the solvent. These correction steps ensured that any non-uniformity of the sample under shear conditions in the VFD was properly accounted for in the processed SANS data. For modelling the data, a Gaussian coil form-factor was used. The sample thickness at a rotational speed of 6550 rpm was measured with the DINGO neutron imaging instrument at ANSTO.[20] The instrument is located at the thermal neutron beam port HB2. The high-intensity configuration, corresponding to a L/D ratio of 500 (where L is the distance between the beam collimator to the image plane, and D the diameter of the collimator) and featuring a thermal flux of 5 × 10^7 neutrons cm^{-2} s^{-1}, was chosen for this study. The detector system was equipped with an Andor NEO 5.5 sCMOS, 16 bit, 2560(w) × 2160(h) pixels sensor coupled with a Carl Zeiss lens with a fixed focal length of 50 mm to yield images with a pixel size of ≈67 μm. A 100 μm-thick ZnS/^{6}LiF scintillation screen was utilised for

the acquisition of radiographic images that were carried out with an exposure time of 1 s. Flat field normalization with dose correction, dark current subtraction, and denoising were applied to the raw data with ImageJ software.

3 Results and discussion

The high-resolution radiographs obtained through neutron imaging have previously been used for the *in situ* measurement of film thicknesses in the VFD.[13,21] In this study, radiographic images of the VFD with an empty tube were used as calibration standards to determine film thickness (Fig. 2). The corrected radiographs, adjusted using open beam images to account for inhomogeneous beam intensity at the VFD position (Fig. 3) show that the film thickness for 1 mL of PEG was generally more than >30% greater than that for 1 mL of the ATPS at the same distance from the bottom of the tube (Fig. 2d). A rotational speed of 6550 rpm was chosen, as it is the optimal speed for enhanced protein purification applications.[1] Upon stopping the rotation, phase separation was revealed, with a darker top phase (PEG-rich, $\rho_{PEG} = 1.15$ g mL^{-1}) and a lighter bottom phase (potassium phosphate-rich, $\rho_{aqueous\ photassium\ phosphate} = 1.39$ g mL^{-1}) (Fig. 3d). Our previous findings demonstrated that phase separation occurs during the spin-up and rotations.[22] However, investigating this separation process during rotation presents challenges for both neutron imaging (Fig. 3c) and high-speed camera observation (Fig. S1). This limitation arises primarily because each neutron image represents an average over thousands of rotations, and imperfections in the tube geometry cause variations in film thickness along the circumference. Additionally, vibrations during rotation further average out these differences, making the film appear uniformly thick. In rotating systems, the less dense liquid often forms an internal layer that can visually overlap with the denser outer layer. This overlap produces a blended appearance that obscures the phase boundary. Together, these factors present challenges for both neutron imaging and high-speed video, which are currently limited in their ability to capture phase separation in actively rotating systems such as the VFD.

Given the current limitations of visualising phase separation during system rotation, alternative techniques are required to probe the underlying mechanisms. SANS measurements have previously been used to explore the structural characteristics of PEG ($M_n = 400$–20000) in neat D$_2$O and its interactions with salt solutions of different ionic strengths.[23,24] In addition, when complexed with sodium lauryl sulphate, PEG adopts a spherical/ellipsoidal conformation wrapping around micelles.[25] Previous SANS studies in a stationary cuvette at low PEG concentrations (mass fraction of <2%) indicated that PEG molecules behave as Gaussian coils.[23] To further investigate the mechanism of spontaneous phase separation in the present system, SANS measurements were conducted *in situ* for the APTS in the VFD. For consistency, data collected in the
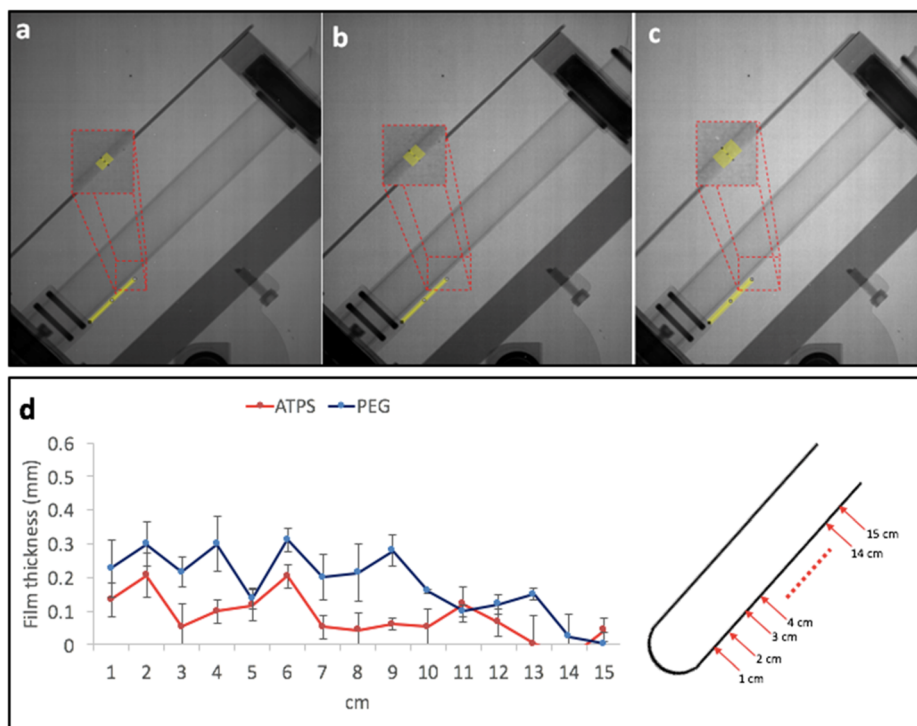

Fig. 2 VFD neutron radiographic image. (a) Reference empty VFD; inset: sidewall of the tube. (b) 1 mL of 6.375% (w/w) PEG in the VFD at 6550 rpm, $\theta = +45°$; inset: sidewall of the VFD tube and the liquid thin film, imaged 3 cm from the bottom of the tube. (c) 1 mL of the ATPS containing 6.375% (w/w) PEG and 13.51% (w/w) potassium phosphate in the VFD at 6550 rpm, $\theta = +45°$; inset: sidewall of the VFD tube and liquid thin film. (d) Film thicknesses (mm) for 1 mL of PEG and 1 mL of the ATPS, as measured along the VFD tube at 1 mm increments from the bottom. At least five measurements were conducted, and the error bars represent the mean ± standard deviation of each experimental conditions.
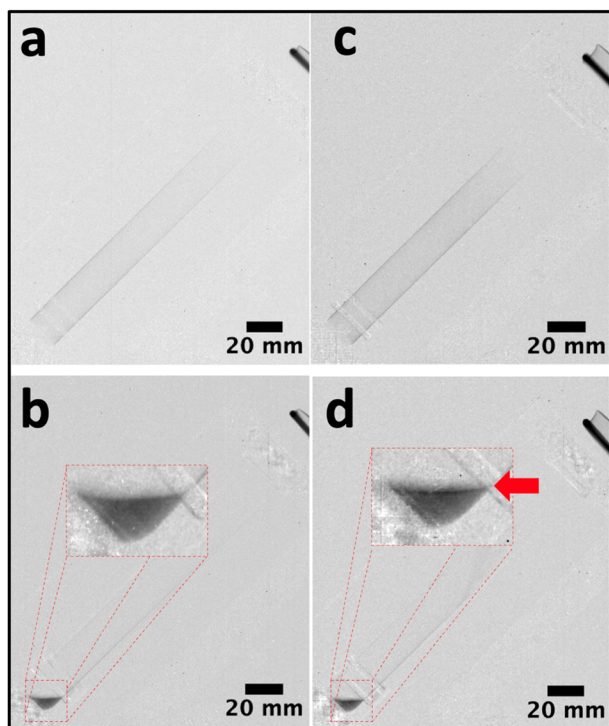
Fig. 3 Neutron imaging of PEG and the ATPS in the VFD under pulsed operation; the image of the empty VFD tube was subtracted to enhance visualization of the liquid phases. (a) 6.375% (w/w) PEG in the VFD at 6550 rpm, $\theta = +45°$. (b) 6.375% (w/w) PEG immediately after the VFD stopped rotating, showing a single liquid phase. (c) ATPS of 6.375% (w/w) PEG and 13.51% (w/w) potassium phosphate in the VFD at 6550 rpm. (d) ATPS of 6.375% (w/w) PEG and 13.51% (w/w) potassium phosphate immediately after the VFD stopped rotating, showing two separated phases. SANS experiments were performed on PEG dissolved in D_2O and the potassium phosphate mixture in H_2O, aiming to achieve sufficient neutron scattering contrast for the measurements.

stationary quartz cell or quartz VFD tube were background corrected using D_2O. Petrenko et al.[26] reported an upturn of the scattering at low q-values due to the structure-factor effect at higher PEG concentrations (>3%). This upturn, which is related to polymer chain clustering,[26] was observed for all experiments in the VFD (PEG alone and the ATPS), but not for PEG alone in the stationary cuvette (Fig. 4a). The VFD might trigger nanoscale clustering of PEG molecules. For VFD-processed PEG molecules, distinct differences were observed at low and mid q-values. Both VFD samples exhibited steeper slopes at low q-values compared to the cuvette measurement. Additionally, in the mid q region, both VFD samples displayed a different profile, with intensity falling off more rapidly than that of PEG in the cuvette. According to Pedersen et al.,[27] for PEG concentrations below 3% w/w, the scattering curve can be approximated by (eqn (1)) for non-interacting Gaussian coils

$$I(q) = I(0)P_{GC}(q) + B = I(0)\frac{2\left[e^{-q^2 R_g^2} + q^2 R_g^2 - 1\right]}{(q^2 R_g^2)^2} + B \quad (1)$$

where $P_{GC}(q)$ is the form factor of the Gaussian coil, R_g is the radius of gyration, $I(0)$ is the forward scattering intensity and B

is the incoherent neutron background. At PEG concentrations above 3% w/w, the scattered intensity can be treated using the random phase approximation (eqn (2)).[26]

$$I(q) = I(0)\left[P_{GC}(q) - \frac{A}{I(0)}P_{GC}(q)^2\right] + B \quad (2)$$

where A is a parameter proportional to the second virial coefficient, describing the effective strength and nature (repulsive or attractive) of the monomer–monomer interaction. The resulting fit parameters are summarised in Table 1.

According to Rubinson et al.,[28] the compressibility of PEG allows it to adopt different conformations, namely Gaussian coils or flat plates, depending on intermolecular distance and PEG concentration. In the present study, PEG molecules exhibited Gaussian coil behaviour during VFD processing, even under high shear stress at 6550 rpm.[5] Notably, PEG molecules processed in the VFD showed a significantly larger R_g value (16.70 Å) than those in a stationary cuvette (12.78 Å), as shown in Table 1, indicating that shear flow promotes PEG coils' expansion. When PEG (6.375%, w/w) was mixed with aqueous potassium phosphate (13.51%, w/w) to form an ATPS, structural arrangements were observed (Fig. 4a). These changes are attributed to enhanced intermolecular interactions with potassium phosphate, particularly at the broadened interface formed during VFD processing. In this system, the R_g decreased slightly to 15.80 Å, suggest a modest contraction compared to PEG alone in the VFD, yet still more extended than under static conditions. Overall, PEG adopts its most expanded conformation under VFD shear, with slight compaction in the presence of salt, and minimal extension in the absence of shear. This behaviour reflects subtle changes in PEG conformation due to salt and shear-induced interactions, without evidence of shear-induced degradation, as indicated by the comparable R_g values of PEG-rich top phases obtained via both VFD and conventional separations (Fig. 4b).

This expansion is further supported by the A value derived from SANS (Table 1), which reflects the strength of intermolecular interactions. Notably, the A value for PEG processed in the VFD is the highest among all conditions, indicating the strongest intermolecular interactions under shear. However, when PEG is part of an ATPS and processed in the VFD, the A value drops significantly, suggesting much weaker interactions. This contrast highlights the disruptive influence of the ATPS environment on PEG clustering under the shear. PEG is known to form clusters through hydrogen bonding and surface adsorption,[29] but under the unique flow dynamics of the VFD, these clusters are destabilised. Centrifugal force and the slight density difference between the two phases drive phase separation into a thin film along the tube walls.[22] The inclination of the tube further increases the interface area between the two phases.[22] These combined effects—amplified shear, increased interfacial area, and fluid mechanical instabilities promote the dissociation of PEG coils. Furthermore, the elevated ionic strength from potassium phosphate may weaken hydrogen bonds within the coils, allowing PEG coils to expand. This mechanistic insight helps explain the observed reduction in intermolecular interaction (A value) and supports the increased
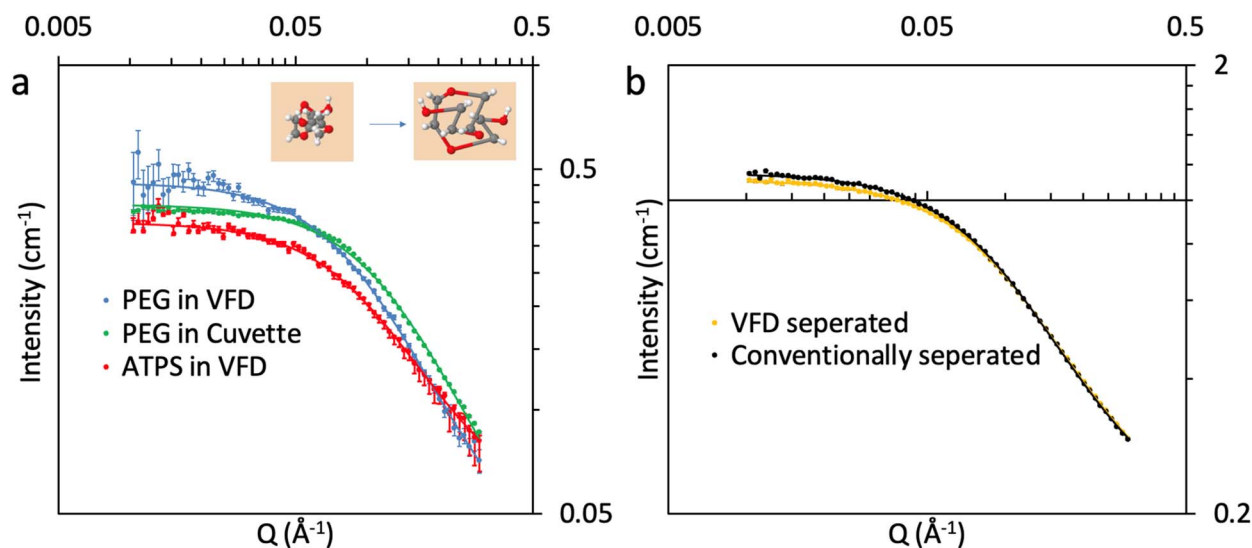
Fig. 4 (a) SANS data for 6.375% (w/w) PEG in the VFD at 6550 rpm, $\theta = +45°$; 6.375% (w/w) PEG in a stationary cuvette; and the ATPS of 6.375% (w/w) PEG and 13.51% (w/w) potassium phosphate in the VFD at 6550 rpm, $\theta = +45°$. (b) SANS data (measured in a stationary cuvette) for the top phases obtained by VFD and conventional separation. The high noise levels in the VFD data are due to the small sample thickness and higher background level compared to the measurement taken from a stationary quartz cuvette. The solid lines in the corresponding colours indicate the fitted curves for each condition. Inset: the shear flow generated in the VFD facilitates the expansion of PEG coils, enhancing their conformational flexibility.

Table 1 Data parameters of different samples, as derived from the SANS data. The parameters were obtained by fitting the scattering data using the Debye model, which describes the form factor of a Gaussian polymer coil

Sample	$I(0)$, cm^{-1}	R_g, Å	A
PEG in VFD	0.045 ± 0.002	16.7 ± 0.2	0.398 ± 0.002
PEG in cuvette	0.042 ± 0.0004	12.78 ± 0.03	0.348 ± 0.0004
ATPS in VFD	0.061 ± 0.002	15.8 ± 0.2	0.283 ± 0.002
Conventionally separated top phase	0.225 ± 0.0005	15.67 ± 0.02	0.9 ± 0.0007
VFD separated top phase	0.225 ± 0.0005	15.16 ± 0.02	0.862 ± 0.0006

R_g measured in the ATPS-VFD condition compared to static systems.

4 Conclusions

This study has demonstrated that the application of thin film shear *via* VFD significantly accelerates the phase separation of PEG and aqueous potassium phosphate ATPS. This process is otherwise slow in conventional batch processing. Using *in situ* SANS, we have elucidated the real-time structural changes of PEG molecules under VFD rotation. The PEG molecules adopt a Gaussian coil configuration, both alone in solution and in the APTS, indicating that the general structure of PEG is maintained under shear and in the presence of potassium phosphate. The decrease in R_g in the presence of potassium phosphate under shear indicates a contraction of PEG polymer chains. These insights offer a mechanistic understanding of polymer–salt interactions and shear-induced structural transitions in biphasic systems. Notably, this work establishes a robust platform for real-time monitoring of molecular dynamics in ATPS using neutron-based techniques. Future

directions could involve systematically increasing the liquid volume and adjusting the ratio of the mixture within the VFD tube to enhance contrast, as well as exploring alternative phase combinations. Such approaches may improve imaging resolution and facilitate real-time monitoring of these systems through more imaging techniques. The findings have broad implications for enhancing the efficiency of biphasic separation processes, with potential applications in bioseparations, materials processing, and advanced fluidics-based purification strategies.

Conflicts of interest

There are no conflicts to declare.

Data availability

The data supporting the findings of this study, including raw and processed neutron scattering and imaging data, are available from the corresponding author upon reasonable request. Additional processed datasets and analysis scripts used to

generate figures and tables in this manuscript can be requested from the authors.

Supplementary information: ATPS behaviour in the VFD as monitored using a high-speed camera. See DOI: **https://doi.org/10.1039/d5mr00093a**.

Acknowledgements

References

1 X. Luo, P. Smith, C. L. Raston and W. Zhang, *ACS Sustain. Chem. Eng.*, 2016, **4**, 3905–3911.

2 K. H. Kroner, H. Schütte, W. Stach and M. R. Kula, *J. Chem. Technol. Biotechnol.*, 1982, **32**, 130–137.

3 K. Selber, F. Tjerneld, A. Collén, T. Hyytiä, T. Nakari-Setälä, M. Bailey, R. Fagerström, J. Kan, J. van der Laan, M. Penttilä and M.-R. Kula, *Process Biochem.*, 2004, **39**, 889–896.

4 H. Yuan, Y. Liu, W. Wei and Y. Zhao, *J. Fluid Eng.*, 2015, **2015**, 1–10.

5 J. Britton, K. A. Stubbs, G. A. Weiss and C. L. Raston, *Chem. Eur J.*, 2017, **23**, 13270–13278.

6 X. Chen, J. F. Dobson and C. L. Raston, *Chem. Commun.*, 2012, **48**, 3703–3705.

7 K. Vimalanathan, J. R. Gascooke, I. Suarez-Martinez, N. A. Marks, H. Kumari, C. J. Garvey, J. L. Atwood, W. D. Lawrance and C. L. Raston, *Scientific Reports*, 2016, **6**, 22865.

8 T. Alharbi, K. Vimalanathan, W. D. Lawrance and C. Raston, *Carbon*, 2018, **140**, 428–432.

9 T. M. D. Alharbi, K. Vimalanathan, I. K. Alsulami and C. L. Raston, *Nanoscale*, 2019, **11**, 21394–21403.

10 X. Luo, A. H. M. Al-Antaki, D. P. Harvey, Y. Ruan, S. He, W. Zhang and C. L. Raston, *ACS Appl. Mater. Interfaces*, 2018, **10**, 27224–27232.

11 J. Britton, L. M. Meneghini, C. L. Raston and G. A. Weiss, *Angew. Chem., Int. Ed.*, 2016, **55**, 11387–11391.

12 J. Britton and C. L. Raston, *RSC Adv.*, 2015, **5**, 2276–2280.

13 M. Jellicoe, A. Igder, C. Chuah, D. B. Jones, X. Luo, K. A. Stubbs, E. M. Crawley, S. J. Pye, N. Joseph, K. Vimalananthan, Z. Gardner, D. P. Harvey, X. Chen, F. Salvemini, S. He, W. Zhang, J. M. Chalker, J. S. Quinton, Y. Tang and C. L. Raston, *Chem. Sci.*, 2022, **13**, 3375–3385.

14 T. Alharbi, M. Jellicoe, X. Luo, K. Vimalanathan, I. K. Alsulami, B. S. Al Harbie, A. Igder, F. A. J. Alrashaidi, X. Chen, K. Stubbs, J. M. Chalker, W. Zhang, R. A. Boulos, D. B. Jones, J. Quinton and C. L. Raston, *Nanoscale Adv.*, 2021, **3**, 3064.

15 E. Perfect, C. L. Cheng, M. Kang, H. Z. Bilheux, J. M. Lamanna, M. J. Gragg and D. M. Wright, *Earth-Sci. Rev.*, 2014, **129**, 120–135.

16 S. He, N. Joseph, M. Mirzamani, S. J. Pye, A. H. M. Al-anataki, A. E. Whitten, Y. Chen, H. Kumari and C. L. Raston, *npj Sci. Food*, 2020, **4**, 12.

17 H. Kumari, S. R. Kline, S. R. Kennedy, C. Garvey, C. L. Raston, J. L. Atwood and J. W. Steed, *Chem. Commun.*, 2016, **52**, 4513–4516.

18 N. Joseph, M. Mirzamani, T. Abudiyah, A. H. M. Al-Antaki, M. Jellicoe, D. P. Harvey, E. Crawley, C. Chuah, A. E. Whitten, E. P. Gilbert, S. Qian, L. He, M. Z. Michael, H. Kumari and C. L. Raston, 2024, **6**, 1202–1212.

19 G. Lancz, M. Avdeev, V. Petrenko, V. Garamus, M. Koneracká and P. Kopčanský, *Acta Phys. Pol., A*, 2010, **118**, 980.

20 U. Garbe, T. Randall, C. Hughes, G. Davidson, S. Pangelis and S. J. Kennedy, *Phys. Procedia*, 2015, **69**, 27–32.

21 T. E. Solheim, F. Salvemini, S. B. Dalziel and C. L. Raston, *Scientific Reports*, 2019, **9**, 2817.

22 E. Leivadarou, *Rotating Thin Films: the Vortex Fluidic Device*, 2019, DOI: **10.17863/CAM.40943**.

23 G. Lancz, M. Avdeev, V. Petrenko, V. Garamus, M. Koneracká and P. Kopčanský, *Acta Phys. Pol.*, 2010, **118**, 980–982.

24 K. A. Rubinson and S. Krueger, *Polymer*, 2009, **50**, 4852–4858.

25 C. Ade-Browne, A. Dawn, M. Mirzamani, S. Qian and H. Kumari, *J. Colloid Interface Sci.*, 2019, **544**, 276–283.

26 V. Petrenko, L. Bulavin, M. Avdeev, V. Garamus, M. Koneracka and P. Kopcansky, *Macromol. Symp.*, 2014, **335**, 20–23.

27 J. S. Pedersen, *Adv. Colloid Interface Sci.*, 1997, **70**, 171–210.

28 K. A. Rubinson and J. Hubbard, *Polymer*, 2009, **50**, 2618–2623.

29 B. Hammouda, D. Ho and S. Kline, *Macromolecules*, 2002, **35**, 8578–8585.